Constrained Ensemble Kalman Filter for Distributed Electrochemical State Estimation of Lithium-Ion Batteries

(article starts on next page)

Constrained Ensemble Kalman Filter for Distributed Electrochemical State Estimation of Lithium-Ion Batteries

Yang Li, *Member, IEEE,* Binyu Xiong, *Member, IEEE,* Don Mahinda Vilathgamuwa, *Fellow, IEEE,*
Zhongbao Wei, *Member, IEEE,* Changjun Xie, *Member, IEEE,* and Changfu Zou *Member, IEEE*

Abstract—This article proposes a novel model-based estimator for distributed electrochemical states of lithium-ion (Li-ion) batteries. Through systematic simplifications of a high-order electrochemical-thermal coupled model consisting of partial differential-algebraic equations, a reduced-order battery model is obtained that features an equivalent circuit form and captures local state dynamics of interest inside the battery. Based on the physics-based equivalent circuit model, a constrained ensemble Kalman filter (EnKF) is pertinently designed to detect internal variables such as the local concentrations, overpotential, and molar flux. To address slow convergence issues due to weak observability of the battery model, the Li-ion's mass conservation is judiciously considered as constraints in the estimation algorithm. The estimation performance is comprehensively examined under a wide operating range. It demonstrates that the proposed EnKF-based nonlinear estimator is able to accurately reproduce the physically-meaningful state variables at a low computational cost and is significantly superior to its prevalent benchmarks for online applications.

Index Terms—Ensemble Kalman filter (EnKF), lithium-ion (Li-ion) batteries, physics-based equivalent circuit model (PB-ECM), state estimation.

I. Introduction

DUE to the distinct advantages of high power and energy densities, low self-discharge rate, favorable modularity, and recent fast decline in cost, lithium-ion (Li-ion) batteries have become the leading electrochemical energy storage technology. Consequently, they are widely used in applications ranging from portable electronic devices to electric vehicles (EVs) and modern power systems [1]–[3]. The increasing need for wider operating ranges, higher safety and longer service life of the Li-ion batteries demands health-aware battery management systems (HBMS). To achieve HBMS, a fundamental step is to accurately monitor health-related states of the batteries, such as the Li-ion concentrations, overpotentials, internal resistances, and internal temperatures. However, none of these variables are physically measurable using available commercial sensing technology [3].

Model-based state estimation is one of the most effective techniques to predict the internal dynamic behaviors, which requires an accurate and efficient mathematical model of the Li-ion batteries. Having simple structure, the equivalent circuit models (ECMs) are easy to implement and preferable for engineers without much prior knowledge on electrochemistry [4]. The lumped parameters of ECMs are easy to identify and numerous well-developed model analysis methods have been integrated into existing tools to facilitate the design of the control system. However, conventional ECMs are lack of physical insights and, therefore, are not applicable to estimate the above health-related states.

In contrast, derived from the underlying electrochemical and thermodynamic principles, physics-based models are capable of providing more valuable and essential information for predicting battery health [5], [6] and for designing optimal control strategies [7], [8]. The pseudo two-dimensional (P2D) model has been widely accepted as the most accurate physics-based Li-ion battery model in the BMS field [9]. However, as P2D model is described by a set of coupled and highly nonlinear partial differential-algebraic equations (PDAEs), it is impractical to implement such a model in HBMS for online operation due to the prohibitively high computational cost.

To avoid such difficulty, extensive research efforts have been made to simplify the P2D model for battery state estimation purpose. For example, the single particle model (SPM) describes each electrode of the cell in a lumped manner with the electrolyte and temperature dynamics ignored [10], and it has been used for various state of charge (SOC) estimators design [11]–[14]. For improved accuracy, such a model was then extended to incorporate the electrolyte dynamics in [15], [16] and capture thermal dynamics in [17], respectively. However, the "lumped particle" assumption for each electrode underpinning these models holds only under low to moderate current rates but can be largely violated under other conditions, particularly when the battery has thick electrodes. The limitation of SPM and its variants has motivated the development of simplified P2D models with distributed electrode behaviors, such as the spatially discretized models [18]–[20], and the polynomially approximated model [21].

Yang Li is with the School of Automation, Wuhan University of Technology, Wuhan 430070, China, and also with the Department of Electrical Engineering, Chalmers University of Technology, 41296 Gothenburg, Sweden (e-mail: yang.li@whut.edu.cn, yangli@ieee.org).

Binyu Xiong and Changjun Xie are with the School of Automation, Wuhan University of Technology, Wuhan 430070, China. (e-mail: bxiong2@whut.edu.cn; jackxie@whut.edu.cn).

Don Mahinda Vilathgamuwa is with the School of Electrical Engineering and Robotics, Queensland University of Technology, Brisbane, QLD 4001, Australia (e-mail: mahinda.vilathgamuwa@qut.edu.au).

Zhongbao Wei is with the National Engineering Laboratory for Electric Vehicles, School of Mechanical Engineering, Beijing Institute of Technology, Beijing 100081, China (e-mail: weizb@bit.edu.cn).

Changfu Zou is with the Department of Electrical Engineering, Chalmers University of Technology, 41296 Gothenburg, Sweden (e-mail: changfu.zou@chalmers.se).

However, these models are described by differential-algebraic equations, and iterative methods are needed to solve them. To mitigate the computational burden, transfer functions together with the residual grouping [22] or a discrete realization algorithm [23] were used to develop reduced physics-based models. Nevertheless, linearization based on certain SOC and state values has to be performed before transferring all governing equations from time domain to frequency domain. The accuracy of the obtained models is significantly reduced for applications with a wide SOC range and high current rates, such as for EV fast charging. Furthermore, these physics-based models commonly have a large number of parameters which are difficult to identify. Hence, the practicability and applicability of the reduced P2D models have not been fully justified for battery state estimation.

To address the problems of electrochemical models, researchers have recently revisited ECMs and proposed physics-based ECMs (PB-ECMs) with the capability of describing the distributed battery characteristics [24]–[26]. The physical natures, including Li-ion diffusion, mass conservation, and temperature and degradation dynamics, can be well explained using PB-ECMs [24]. In general, ECMs have much less parameters than electrochemical models, and consequently, its identification procedure can be less tedious [25]. Inspired by this, a general PB-ECM framework has been developed and exhibited high efficiency and accuracy [26]. However, the model adaptation and order reduction criteria for PB-ECMs have not yet been established and demonstrated for the distributed state estimation.

The first contribution of the present work is to extend the PB-ECM framework of [26] from three aspects for estimating the distributed electrochemical states of Li-ion batteries. First, a generalized sub-circuit for solid-phase diffusion processes will be developed by applying Padé approximation. This will offer extra freedom to the model framework through which the model validity can be maintained at different operating ranges by tuning parameters of Padé approximation. Second, by fully considering the smallness of temperature gradient across the cell thickness direction [27], a lumped heat transfer model and a distributed heat generation model will be fused to describe the coupled electrochemical-thermal behaviors. In addition, the criteria to determine the system order will be established for low-cost and high-fidelity estimator design.

Building upon distributed parameter models, research efforts have been devoted to battery state estimation. To predict the local state behaviors, Smith et al. [22] designed a linear Kalman filter based on an impedance model derived by linearizing a reduced P2D model at 50% SOC. To capture battery nonlinear dynamics, different kinds of extended Kalman filters (EKFs) have been deployed together with various reduced-order P2D models [19]–[21], [23]. However, the implementation of EKFs requires labor-intensive derivation and computationally heavy calculation of high-dimensional Jacobian matrices of the physics-based models. To sidestep the Jacobian matrices, Tulsyan et al. [28] proposed a particle filter (PF) based on a reformulated P2D model, while Marelli and Corno [29] designed a unscented Kalman filter (UKF) based on a discretized P2D model and the finite different method.

Nevertheless, due to the requirement to online calculate a large number of particles/sigma points and high-dimensional covariance matrices, as well as resampling, PF and UKF are still intractable for many HBMS.

The ensemble Kalman filter (EnKF) is a data assimilation technique proposed by Evensen [30] and has been successfully applied, such as in weather forecast, image reconstruction, and ocean modeling. In these fields, EnKF is capable of dealing with high-dimensional spatially-discretized models, where there are more state variables than measurements. It applies Monte Carlo method to the conventional Kalman filter, and the basic idea is to use a low-rank approximation of the large-size covariance matrix. Because there is no need to derive separate covariance matrices as in UKF and PF, and no need to calculate Jacobian as in EKF, EnKF is very computationally efficient [31]. In addition, EnKF has demonstrated excellent performance in robustness and addressing model nonlinearities. These advantages make EnKF a promising candidate to solve the battery estimation problem.

To estimate the distributed electrochemical states of a Li-ion cell, a particular concern is how to maintain mass conservation of Li-ions. Process and measurement noises inherently existed in battery operation can lead to the loss of mass conservation. Consequently, the estimation accuracy can be reduced significantly, potentially leading to biased estimates [32]. To address this problem, nonlinear constrained Kalman filters have established, in which complex optimization problems are solved online to obtain the Kalman gain [33]. To avoid online nonlinear optimization, Strum et al. [21] considered a constraint of mass conservation in the initialization step of their EKF-based estimators, and Marelli and Corno [29] proposed a soft-constrained UKF to maintain the mass conservation. Considering the drawbacks of EKF and UKF for PB-ECMs, it is of great importance to investigate how to efficiently incorporate physical constraints into the EnKF algorithm.

The *second contribution* of this work is to bridge the identified research gap by proposing an EnKF-based estimation algorithm for the distributed electrochemical states based on an adaptive and control-oriented PB-ECM. Physical constraints will be incorporated into the EnKF to ensure the satisfaction of Li-ion mass conservation in both the electrolyte and solid phase. This will also ameliorate the model observability. Furthermore, based on the initial guess of the SOC range, a simple ensemble initialization approach will be proposed to speed up the convergence process for Li-ion battery estimation.

II. DEVELOPMENT OF THE CONTROL-ORIENTED PB-ECM-T FOR LI-ION BATTERIES

In this section, a control-oriented PB-ECM will be developed for distributed state estimation. To begin with the model development, the model framework from [26] is recapped in Section II-A.

A. A Distributed-Parameter PB-ECM Framework

The circuit structure of the distributed-parameter PB-ECM framework is shown in Fig. 1. It was developed by applying the approaches, including change of variables, electrical analogy,
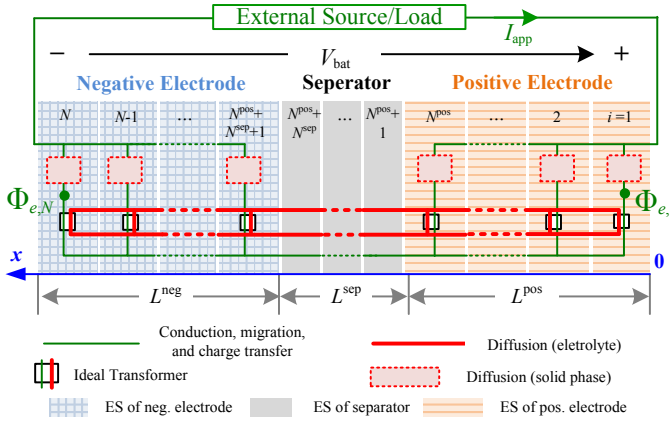
Fig. 1.   Schematic of the physics-based equivalent circuit derived from P2D model of Li-ion cells. The circuit elements such as the resistors and capacitors are not shown.
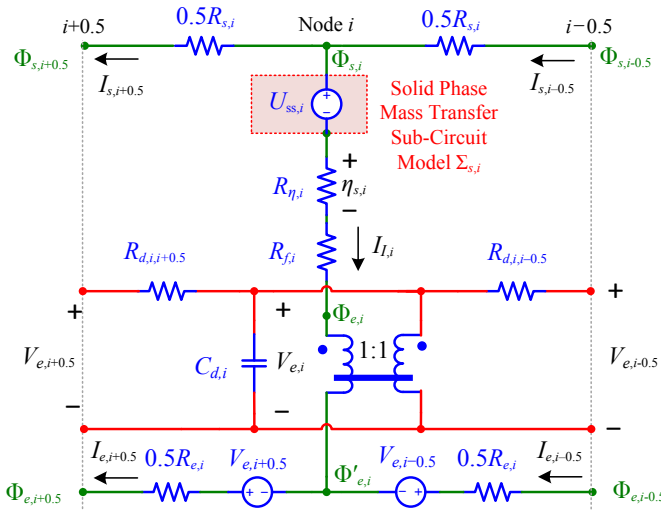

Fig. 2.   A generic ES of the PB-ECM of the Li-ion battery model. The conduction (charge conservation) sub-circuit (green lines) and the electrolyte diffusion (mass conservation) sub-circuit (red lines) are connected via an ideal transformer with turns ratio 1:1.

and finite volume method (FVM) to an electrochemical P2D model of Li-ion cells. This circuit emulates the sandwich structure of the Li-ion cell, including the positive electrode, the negative electrode, and the separator in between. As indicated in Fig. 1, it consists of sub-circuits which present internal processes such as diffusion, migration, conduction, charge transfer, etc. Standard circuit elements such as resistors (R), capacitors (C), and ideal transformers are used to construct the PB-ECM. As shown in Fig. 1, the PB-ECM is divided into $N = N^{\text{pos}} + N^{\text{sep}} + N^{\text{neg}}$ *elementary sections* (ESs) as a consequence of spatial discretization along the horizontal axis (x-direction). Here, N^{pos}, N^{sep}, and N^{neg} are the numbers of ESs for the positive electrode, the separator, and the negative electrode, respectively. A generalized circuit structure for the ith ES is depicted in Fig. 2.

In Fig. 2, the subscript $i \in \{1, 2, \cdots, N\}$ represents the variables or components at the central node of the ES, and $i \pm 0.5$ represents the variables or components at the edges of the ES. Φ_s and Φ_e are the solid phase and the electrolyte

potentials, respectively, I_s and I_e are the solid phase and the electrolyte currents, respectively, U_{ss} is the equilibrium potential of the electrode, η_s is the activation or charge transfer overpotential, and I_I represents the intercalation current. Furthermore, R_η, R_s, R_e, and R_f are the charge-transfer resistance, solid-phase resistance, electrolyte resistance, and SEI film resistance, respectively.

Note that for an ES located in the separator domain, the circuit shown in Fig. 2 can be simplified by considering zero intercalation current (i.e., $I_I = 0$) and thus the solid-phase-related branches and elements can be removed. In addition, the ES at the boundaries of respective domains can also be simplified by considering the boundary conditions of the rigorous P2D model. When interconnecting all the N ESs to construct the entire PB-ECM, the resistors such as R_e, R_s, and R_d can be combined with those in the adjacent ES. Furthermore, the controlled voltage sources $V_{e,i+0.5}$ and $V_{e,i-0.5}$ are removable as they are effectively canceled out by those in the adjacent ES.

B. Subcircuit for the Solid-Phase Diffusion Process

In Fig. 2, the equilibrium potential $U_{\text{ss},i}$ is represented as a voltage source controlled by the intercalation current $I_{I,i}$. It is originally governed by the diffusion equation of Fick's second law expressed in the spherical coordinate of the solid particle. Instead of simplifying this equation using a fixed-order circuit structure based on polynomial profile approximation proposed in [26], a generalized subcircuit $\Sigma_{s,i}$ will be developed in this subsection for a wide range of operation based on Padé approximation. First, by applying M-order Padé approximation to the solid-phase diffusion equation, a linear relationship can be established between the intercalation molar flux $j_{I,i}$ and the surface concentration $c_{\text{ss},i}$ in the solid phase, i.e., [34]

$$\frac{c_{\text{ss},i}(s)}{j_{I,i}(s)} = \frac{a_0 + a_1 s + a_2 s^2 \cdots + a_{M-1} s^{M-1}}{1 + b_2 s + b_2 s^2 \cdots + b_M s^{M-1}} \frac{1}{s}. \quad (1)$$

Here $j_{I,i}$ is proportional to $I_{I,i}$, i.e., $j_{I,i} = I_{I,i}/(Al_i a_{s,i} F)$, where F is the Faraday's constant, A is the electrode cross section area, $a_{s,i}$ is the electrode specific area, and l_i is the thickness of the ith ES. $a_0, a_1, \cdots, a_{M-1}$, and $b_2, \cdots, b_M$ are the Padé coefficients. These coefficients can be determined using the method given in [34], [35]. Note that the spatial index i attached to the Padé coefficients is dropped in this subsection for the sake of readability.

Similarly, a linear relationship between $j_{I,i}$ and the volume-averaged concentration $c_{s,\text{avg},i}$ exists [34]

$$\frac{c_{s,\text{avg},i}(s)}{j_{I,i}(s)} = -\frac{3}{R_{p,i} s} \quad (2)$$

where $R_{p,i}$ is the radius of the particle at the ith ES.

In order to derive an analogy to electrical circuit, the following realization is proposed for (1) by choosing a set
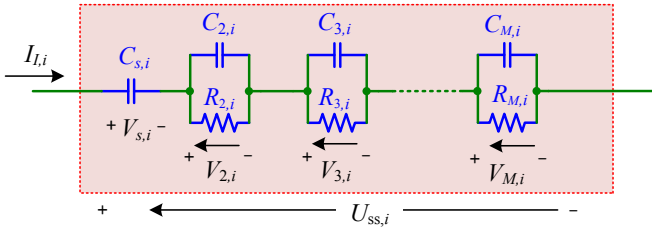
Fig. 3. Equivalent RC circuit for the diffusion equation in solid phase based on Mth order Padé approximation.

of state variables such that the state-space representation is

$$
\begin{bmatrix} \dot{c}_{s,\text{avg},i} \\ \dot{\tilde{c}}_{s,2,i} \\ \vdots \\ \dot{\tilde{c}}_{s,M,i} \end{bmatrix} = \begin{bmatrix} 0 & 0 & \cdots & 0 \\ 0 & \alpha_{22} & \cdots & 0 \\ \vdots & \vdots & \ddots & 0 \\ 0 & 0 & 0 & \alpha_{MM} \end{bmatrix} \begin{bmatrix} c_{s,\text{avg},i} \\ \tilde{c}_{s,2,i} \\ \vdots \\ \tilde{c}_{s,M,i} \end{bmatrix}
$$
$$
+ \begin{bmatrix} -3/R_{p,i} & \beta_2 & \cdots & \beta_M \end{bmatrix}^{\top} j_{I,i} \quad (3a)
$$

$$
c_{\text{ss}} = \overbrace{\begin{bmatrix} 1 & 1 & \cdots & 1 \end{bmatrix}}^{1 \times M} \begin{bmatrix} c_{s,\text{avg}} & \tilde{c}_{s,2} & \cdots & \tilde{c}_{s,M} \end{bmatrix}^{\top} \quad (3b)
$$

where $\tilde{c}_{s,2,i}, \cdots, \tilde{c}_{s,M,i}$ are concentration deviation terms from the volume-averaged concentration $c_{s,\text{avg},i}$. Denoting $\mathbf{A}'$, $\mathbf{B}'$, and $\mathbf{C}'$ as the system matrix, the input matrix, and the output matrix of (3), respectively, the coefficients $\alpha_{22}, \cdots, \alpha_{MM}$ and $\beta_2, \cdots, \beta_M$ in (3a) can be uniquely determined by balancing the equation $c_{\text{ss},i}(s)/j_{I,i}(s) = \mathbf{C}'(s\mathbf{I} - \mathbf{A}')^{-1}\mathbf{B}'$ according to (1) and (3).

Next, applying the following rule of change of state variables, the concentrations are mapped to a set of voltages

$$
U_{\text{ss},i} = V_{s,i} + \sum_{j=2}^{M} V_{j,i} = f_{\text{OCP},i}\left(\frac{c_{s,\text{avg},i} + \sum_{j=2}^{M} \tilde{c}_{s,j,i}}{c_{s,\max,i}}\right) \quad (4)
$$

where $c_{s,\max,i}$ is the maximum theoretical concentration in the solid phase of the ith ES.

Equation (4) consists of M subequations taking account of the equilibrium potential vs. normalized concentration characteristics $f_{\text{OCP},i}(\cdot)$. Note that function $f_{\text{OCP},i}(\cdot)$ is $f_{\text{OCP}}^{\text{pos}}(\cdot)$ for the positive electrode and $f_{\text{OCP}}^{\text{neg}}(\cdot)$ for the negative electrode, respectively. In this way, the state variables are mapped from an M-dimensional concentration space into an M-dimensional voltage space according to a nonlinear transformation. Note that $V_{s,i}$ in (4) equals the open-circuit potential (OCP) of the corresponding electrode at no-load condition. The resultant equivalent circuit $\Sigma_{s,i}$ is shown in Fig. 3.

C. Thermal Model

Note that the parametric values of the circuit elements of the PB-ECM are usually temperature-dependent. A thermal model can be readily incorporated into the PB-ECM to dynamically describe the thermal behaviors of the battery. The heat source equals the heat generated by the various circuit components of the PB-ECM, which is referred to as the heat generation model. As the sandwich structure of Li-ion cells is very thin, the corresponding temperature gradient is small [27]. In light

of this, a lumped heat transfer model is considered to relieve the computational burden for online state estimation. Based on the above discussion, the following thermal model with a lumped heat transfer term and a distributed heat generation term is formulated to describe the battery temperature $T(t)$,

$$
C_T \dot{T}(t) = \frac{T_{\text{amb}} - T(t)}{R_T} + \sum_{i=1}^{N} Q_{T,i}(t) \quad (5)
$$

where C_T is the lumped thermal capacitance, R_T is the lumped thermal resistance, T_{amb} is the ambient temperature, $Q_{T,i}(t)$ is the local heat generation. The battery temperature $T(t)$ is considered an additional state variable to the PB-ECM, and thus the resultant coupled electrochemical-thermal model is denoted PB-ECM-T, while the corresponding P2D model with lumped thermal model is denoted P2D-T model.

D. Determination of Model Complexity of PB-ECM-T

The PB-ECM-T is subject to a complicated mathematical structure, and thus the corresponding model-based estimation algorithms could be computationally intractable when implemented in HBMS. It is interesting to see that the model complexity is completely controlled by the number of ES (N^{pos}, N^{sep}, N^{neg}) and the order M of the Padé approximation. The system order n of this PB-ECM-T is thus the number of the capacitors plus one (temperature state), i.e., $n = (M+1)(N^{\text{pos}} + N^{\text{neg}}) + N^{\text{sep}} + 1$. In this regard, this subsection discusses the underpinning assumptions made on the properties of the battery for further model reduction.

Denoting the ES index sets $\mathcal{S}^{\text{pos}} = \{1, 2, ..., N^{\text{pos}}\}$, $\mathcal{S}^{\text{sep}} = \{N^{\text{pos}}+1, N^{\text{pos}}+2, ..., N^{\text{pos}}+N^{\text{sep}}\}$ and $\mathcal{S}^{\text{neg}} = \{N^{\text{pos}}+N^{\text{sep}}+1, ..., N\}$, the two assumptions are

Assumption 1: Given $\epsilon_1 > 0$, $\exists M^* \in \mathbb{Z}_+$ such that $\forall M \geq M^*$ and $\forall i \in \mathcal{S}^{\text{pos}} \cup \mathcal{S}^{\text{neg}}$, the local equilibrium potential satisfies

$$
\left| \frac{U_{\text{ss}}(x,t) - \left(V_{s,i}(t) + \sum_{j=2}^{M} V_{j,i}(t)\right)}{U_{\text{ss}}(x,t)} \right| < \epsilon_1, \forall t > 0 \quad (6)
$$

where , and $U_{\text{ss}}(x,t)$ represents the local equilibrium potential at horizontal position x of the P2D-T model.

For example, applying the second-order Padé approximation ($M = 2$) according to (1)–(2), and based on (3)–(4), following second-order RC system can be obtained

$$
C_{s,i}\dot{V}_{s,i}(t) = I_{I,i}(t) \quad (7a)
$$
$$
C_{2,i}\dot{V}_{2,i}(t) = -V_{2,i}(t)/R_{2,i} + I_{I,i}(t) \quad (7b)
$$
$$
U_{\text{ss},i}(t) = V_{s,i}(t) + V_{2,i}(t). \quad (7c)
$$

Assumption 2: Given $\epsilon_2 > 0$ and $M > 0$, $\exists N^{\text{pos}*} \in \mathbb{Z}_+$, $\exists N^{\text{sep}*} \in \mathbb{Z}_+$, $\exists N^{\text{neg}*} \in \mathbb{Z}_+$, such that $\forall N^{\text{pos}} \geq N^{\text{pos}*}$, $\forall N^{\text{sep}} \geq N^{\text{sep}*}$, and $\forall N^{\text{neg}} \geq N^{\text{neg}*}$, potential Φ_e satisfies

$$
\left| \frac{\Phi_e(x,t)|_0^{L^{\text{tot}}} - (\Phi_{e,1}(t) - \Phi_{e,N}(t))}{\Phi_e(x,t)|_0^{L^{\text{tot}}}} \right| < \epsilon_2, \forall t > 0 \quad (8)
$$

where $L^{\text{tot}} = L^{\text{pos}} + L^{\text{sep}} + L^{\text{neg}}$ is the thickness of the battery cell, $\Phi_e(x,t)$ represents the local electrolyte potential at position x of the P2D-T model, and $\Phi_{e,1}$ and $\Phi_{e,N}$ are two potentials indicated in Fig. 1 for $i = 1$ and $i = N$, respectively.

E. Summary of the PB-ECM-T

Based upon the results from the above subsections, the detailed description of the PB-ECM-T is determined. According to Kirchhoff's circuit laws, the PB-ECM-T can be readily expressed in a compact continuous-time state-space form, i.e.,

$$\dot{\mathbf{x}}(t) = \mathbf{A}(\mathbf{x}, \mathbf{u}) \cdot \mathbf{x}(t) + \mathbf{B}(\mathbf{x}, \mathbf{u}) \cdot \mathbf{u}(t) =: \mathcal{F}(\mathbf{x}, \mathbf{u}) \quad (9a)$$

$$\mathbf{z}(t) = \mathbf{C}(\mathbf{x}, \mathbf{u}) \cdot \mathbf{x}(t) + \mathbf{D}(\mathbf{x}, \mathbf{u}) \cdot \mathbf{u}(t) =: \mathcal{H}(\mathbf{x}, \mathbf{u}) \quad (9b)$$

where the state vector $\mathbf{x} = [\mathbf{v}_s^\top, \mathbf{v}_e^\top, \mathbf{v}_2^\top, \cdots, \mathbf{v}_M^\top, T]^\top$ includes all the capacitor voltages and the battery temperature, where $\mathbf{v}_s = [V_{s,1}, V_{s,2}, \cdots, V_{s,N}]^\top$, $\mathbf{v}_e = [V_{e,1}, V_{e,2}, \cdots, V_N]^\top$, $\mathbf{v}_2 = [V_{2,1}, V_{2,2}, \cdots, V_{2,N}]^\top$, $\cdots$, and $\mathbf{v}_M = [V_{M,1}, V_{M,2}, \cdots, V_{M,N}]^\top$. The input $\mathbf{u}(t)$ is the applied current $I_{\mathrm{app}}(t)$, and the measurable output $\mathbf{z}(t)$ is the battery terminal voltage $V_{\mathrm{bat}}(t)$. Note that according to Kirchhoff's laws, the matrices $\mathbf{A}$, $\mathbf{B}$, $\mathbf{C}$, and $\mathbf{D}$ in (9) are linear functions of the circuit RC parameters. However, as these RC parameters are also functions of the state vector $\mathbf{x}$ and the input $\mathbf{u}$, the RHS of (9a) and (9b) shall be generally expressed using two nonlinear operators $\mathcal{F}$ and $\mathcal{H}$, respectively. The detail of the PB-ECM-T is provided in the supplementary material. As no algebraic constraints exists in this model, well-established circuit theories can be used for solving the model in computationally efficient ways to obtain all the nodal voltages, branch currents, as well as the terminal voltage.

Many important electrochemical variables can be obtained by solving the PB-ECM-T for HBMS design. For example, the local solid-phase surface concentration $c_{\mathrm{ss},i}(t)$, local volume-averaged concentration $c_{s,\mathrm{avg},i}(t)$, local electrolyte concentration $c_{e,i}(t)$, local activation overpotential $\eta_{s,i}(t)$, local intercalation molar flux $j_{I,i}(t)$, and SOC of the battery can be used to estimate the rate of side reaction which is considered one of the main causes of capacity fade and increase of internal resistance [26]. These information are considered to be the unmeasurable output variables of the PB-ECM-T, i.e.,

$$\mathbf{y} = \left[\mathbf{c}_{\mathrm{ss}}^\top, \mathbf{c}_{s,\mathrm{avg}}^\top, \mathbf{c}_e^\top, \boldsymbol{\eta}_s^\top, \mathbf{j}_I^\top, \mathrm{SOC}\right]^\top =: \mathcal{L}(\mathbf{x}, \mathbf{u}) \quad (9c)$$

where $\mathcal{L}$ is a nonlinear operator, $\mathbf{c}_{\mathrm{ss}}$, $\mathbf{c}_{s,\mathrm{avg}}$, $\boldsymbol{\eta}_s$, and $\mathbf{j}_I$ are the column vectors that contain $c_{\mathrm{ss},i}$, $c_{s,\mathrm{avg},i}$, $\eta_{s,i}$, and $j_{I,i}$, respectively, for $i \in \mathcal{S}^{\mathrm{pos}} \cup \mathcal{S}^{\mathrm{neg}}$, while $\mathbf{c}_e$ is the column vector that contains $c_{e,i}$ for $i \in \mathcal{S}^{\mathrm{pos}} \cup \mathcal{S}^{\mathrm{sep}} \cup \mathcal{S}^{\mathrm{neg}}$. Each of the unmeasurable output variables can be calculated based on the branch currents and nodal voltages of the PB-ECM-T, i.e., [26]

$$c_{\mathrm{ss},i}(t) = c_{s,\max,i} f_{\mathrm{OCP},i}^{-1}\left(U_{\mathrm{ss},i}(t)\right) \quad (10a)$$

$$c_{s,\mathrm{avg},i}(t) = c_{s,\max,i} f_{\mathrm{OCP},i}^{-1}\left(V_{s,i}(t)\right) \quad (10b)$$

$$c_{e,i}(t) = c_e^0 \exp\left(\frac{F}{2R_g t_a^0 T(t)} V_{e,i}(t)\right) \quad (10c)$$

$$\eta_{s,i}(t) = R_{\eta,i} I_{I,i}(t) \quad (10d)$$

$$j_{I,i}(t) = I_{I,i}(t)/(A l_i a_{s,i} F) \quad (10e)$$

$$\mathrm{SOC}(t) = \frac{1}{N^{\mathrm{neg}}} \sum_{i=1}^{N^{\mathrm{neg}}} \frac{c_{s,\mathrm{avg},i}(t) - c_{s,0\%}^{\mathrm{neg}}}{c_{s,100\%}^{\mathrm{neg}} - c_{s,0\%}^{\mathrm{neg}}} \quad (10f)$$

where $f_{\mathrm{OCP},i}^{-1}(\cdot)$ is the inverse function of $f_{\mathrm{OCP},i}(\cdot)$, R_g is the universal gas constant, and t_a^0 is the transference number. The width of the ES l_i can be l^{pos}, l^{sep} and l^{neg}, depending on the domain of the ES. Furthermore, $c_{s,100\%}^{\mathrm{neg}}$ and $c_{s,0\%}^{\mathrm{neg}}$ are the negative electrode solid-phase concentrations at the fully-charged and the fully-discharged states, respectively.

By discretizing (9) in the time domain, e.g. using standard Euler method, a discrete-time nonlinear representation of the PB-ECM-T can be obtained for the controller implementation,

$$\mathbf{x}_k = \mathcal{F}_d(\mathbf{x}_{k-1}, \mathbf{u}_k, \Delta t) \quad (11a)$$

$$\mathbf{z}_k = \mathcal{H}(\mathbf{x}_{k-1}, \mathbf{u}_k) \quad (11b)$$

$$\mathbf{y}_k = \mathcal{L}(\mathbf{x}_{k-1}, \mathbf{u}_k) \quad (11c)$$

where k is the discrete time index, Δt is the time step, $\mathcal{F}_d =: \Delta t \times \mathcal{F} + \mathbf{x}_{k-1}$ is a nonlinear operator derived from $\mathcal{F}$ in (9a), while operators $\mathcal{H}$ and $\mathcal{L}$ are the same as those in (9b) and (9c), respectively. With the initial state vector $\mathbf{x}_0$ and the input sequence $\mathbf{u}_k = I_{\mathrm{app},k}$, (11) can be efficiently solved.

III. STATE ESTIMATION USING CONSTRAINED ENKF

A. Ensemble Kalman Filter

In this section, a distributed state estimator is designed to observe the internal variables (10) of the Li-ion batteries using the PB-ECM-T developed in Section II. Depending on the selection of N^{pos}, N^{sep}, N^{neg}, and M, however, the PB-ECM-T (11) may still exhibit much higher-order nature than the conventional lumped-parameter ECMs, especially for high current applications, such as fast charging of EVs. As such, EnKF is introduced in the following to alleviate the design difficulty and reduce the computational burden.

At the kth time step, an $n \times m$ matrix $\hat{\mathbf{X}}_k$ is defined as an *ensemble of state estimates* with m samples of the states, i.e.,

$$\hat{\mathbf{X}}_k =: \begin{bmatrix} \hat{\mathbf{x}}_{k,1}, & \hat{\mathbf{x}}_{k,2}, & \cdots, & \hat{\mathbf{x}}_{k,m} \end{bmatrix}.$$

The ensemble size m can be much smaller than the dimension n of the state variables, i.e., $m \ll n$. Carrying out the following two steps, the ensemble of the state estimates at the kth time step can be generated:

Step 1 Predict: According to the system equation (11a), predict the ensemble of prior state estimates $\hat{\mathbf{X}}_k^-$ of the current time step based on the ensemble of posterior state estimates $\hat{\mathbf{X}}_{k-1}^+$ of the previous time step, the ensemble of the input vector $\mathbf{U}_k$, and the perturbed process error matrix $\mathbf{W}_k$, i.e.,

$$\hat{\mathbf{X}}_k^- = \mathcal{F}_d(\hat{\mathbf{X}}_{k-1}^+, \mathbf{U}_k, \Delta t) + \mathbf{W}_k. \quad (12a)$$

Each column of $\mathbf{U}_k$ equals the input vector $\mathbf{u}_k$, and each column of $\mathbf{W}_k$ is a randomly generated vector that is normally distributed according to $\mathcal{N}(0, \mathbf{Q})$.

Step 2 Update: Calculate the ensemble of the measurement estimates $\hat{\mathbf{Z}}_k$ according to output equation (11b) of the model, based on the ensemble of prior state estimates $\hat{\mathbf{X}}_k^-$ and $\mathbf{U}_k$,

$$\hat{\mathbf{Z}}_k = \mathcal{H}(\hat{\mathbf{X}}_k^-, \mathbf{U}_k). \quad (12b)$$

Next, calculate the *ensemble Kalman gain* $\mathbf{K}_{e,k}$,

$$\mathbf{K}_{e,k} = \frac{\frac{1}{m-1}\sum_{p=1}^{m}\left(\hat{\mathbf{x}}_{k,p}^{-} - \bar{\mathbf{x}}_{k}^{-}\right)\left(\hat{\mathbf{z}}_{k,p} - \bar{\mathbf{z}}_{k}\right)^{\top}}{\frac{1}{m-1}\sum_{p=1}^{m}\left(\hat{\mathbf{z}}_{k,p} - \bar{\mathbf{z}}_{k}\right)\left(\hat{\mathbf{z}}_{k,p} - \bar{\mathbf{z}}_{k}\right)^{\top} + \mathbf{R}} \quad (12c)$$

where $\mathbf{R}$ is the measurement error covariance, $\hat{\mathbf{x}}_{k,p}^{-}$ is the pth column of $\hat{\mathbf{X}}_{k}^{-}$, $\hat{\mathbf{z}}_{k,p}$ is the pth column of $\hat{\mathbf{Z}}_{k}$, while $\bar{\mathbf{x}}_{k}^{-}$ and $\bar{\mathbf{z}}_{k}$ are the ensemble means of $\hat{\mathbf{X}}_{k}^{-}$ and $\hat{\mathbf{Z}}_{k}$, respectively, i.e.,

$$\bar{\mathbf{x}}_{k}^{-} = \frac{1}{m}\sum_{p=1}^{m}\hat{\mathbf{x}}_{k,p}^{-}, \quad \bar{\mathbf{z}}_{k} = \frac{1}{m}\sum_{p=1}^{m}\hat{\mathbf{z}}_{k,p}. \quad (12d)$$

Next, generate the *perturbed measurement ensemble* $\mathbf{Z}_{k}'$ by

$$\mathbf{Z}_{k}' = \mathbf{Z}_{k} + \mathbf{\Gamma}_{k} \quad (12e)$$

where each column of $\mathbf{Z}_{k}$ equals the measurement vector $\mathbf{z}_{k}$ and each column of $\mathbf{\Gamma}_{k}$ is a randomly generated vector and normally distributed according to $\mathcal{N}(0, \mathbf{R})$.

The ensemble of the posterior state estimates can thus be updated by

$$\hat{\mathbf{X}}_{k}^{+} = \hat{\mathbf{X}}_{k}^{-} + \mathbf{K}_{e,k}(\mathbf{Z}_{k}' - \hat{\mathbf{Z}}_{k}). \quad (12f)$$

Finally, the unmeasurable variables $\mathbf{y}_{k}$ can be estimated by substituting $\hat{\mathbf{X}}_{k}^{+}$ and $\mathbf{U}_{k}$ into (11c), i.e.,

$$\hat{\mathbf{Y}}_{k} = \mathcal{L}(\hat{\mathbf{X}}_{k}^{+}, \mathbf{U}_{k}), \quad \bar{\mathbf{y}}_{k} = \frac{1}{m}\sum_{p=1}^{m}\hat{\mathbf{y}}_{k,p} \quad (12g)$$

where $\hat{\mathbf{y}}_{k,p}$ is the pth column of $\hat{\mathbf{Y}}_{k}$.

It can be seen that the EnKF algorithm of (12) is very simple to design and implement, with the following salient merits:

1) Compared to EKF, there is no need to perform sequential linearization, in which calculating a set of large-size $(n \times n)$ Jacobian matrices online can be extremely heavy for the highly nonlinear coupled battery model.

2) The generation of ensemble is much simpler than that of the sigma points in the UKF, and the ensemble size can also be much smaller than that of the sigma points in the UKF.

3) High-dimensional error covariance matrix $\mathbf{P}_{k} \in \mathbb{R}^{n \times n}$ does not need to be estimated and updated. Denoting the dimension of measurement n_{z}, the complexity of EnKF is $\mathcal{O}(n_{z}^{3} + n_{z}^{2}m + n_{z}m^{2} + nm^{2})$, which is much less than $\mathcal{O}(n^{3})$ of EKF and UKF for $n_{z} \ll n$ and $m \ll n$ [36].

The efficiencies of the EnKF-based estimators will be investigated quantitatively and compared with the UKF-based estimators in Section IV.

B. Proposed EnKF Initialization Method

The selection of the initial ensemble of the state estimates $\hat{\mathbf{X}}_{0}^{+}$ largely affects the performance of EnKF. Improper guess of the initial ensemble can lead to slow convergence to the optimal level of the estimator [37]. The prior knowledge about the SOC level is useful to speed up the convergence process. Although the exact initial mean and covariance of the state is difficult to obtain, a proper guess of the possible range of the initial SOC is normally much more practical. Different from

the other types of Kalman-filter based estimators which only one set of initial state variables can be specified, m different initial state vectors can be selected in the initial state ensemble. If no other prior statistical information is available, the initial state ensemble is assumed uniformly covers an estimated range of SOC from $\text{SOC}_{0}^{\min}$ to $\text{SOC}_{0}^{\max}$. The element in the qth row and the pth column in $\hat{\mathbf{X}}_{0}^{+}$ is set to

$$\hat{\mathbf{X}}_{0}^{+}(q,p) = \begin{cases} f_{\text{OCP}}^{\text{pos}}\left(\frac{c_{s0,p}^{\text{pos}}}{c_{s,\max}^{\text{pos}}}\right), & q \in \{1, 2, ..., N^{\text{pos}}\} \\ f_{\text{OCP}}^{\text{neg}}\left(\frac{c_{s0,p}^{\text{neg}}}{c_{s,\max}^{\text{neg}}}\right), & q \in \{N^{\text{pos}}+1, ..., N^{\text{pos}}+N^{\text{neg}}\} \\ T_{0}, & q = n \\ 0, & \text{otherwise} \end{cases}$$
$$\quad (13a)$$

where T_{0} is the initial temperature, and the initial concentrations $c_{s0,p}^{\text{pos}}$ and $c_{s0,p}^{\text{neg}}$ are

$$c_{s0,p}^{\text{pos}} = (c_{s,0\%}^{\text{pos}} - c_{s,100\%}^{\text{pos}})\text{SOC}_{0,p} + c_{s,100\%}^{\text{pos}} \quad (13b)$$

$$c_{s0,p}^{\text{neg}} = (c_{s,100\%}^{\text{neg}} - c_{s,0\%}^{\text{neg}})\text{SOC}_{0,p} + c_{s,0\%}^{\text{neg}} \quad (13c)$$

$$\text{SOC}_{0,p} = \text{SOC}_{0}^{\min} + \frac{p}{m}(\text{SOC}_{0}^{\max} - \text{SOC}_{0}^{\min}). \quad (13d)$$

C. Extension of EnKF to Incorporate Physical Constraints

By examining the observability of the battery states based on the nonlinear model (11) using the method presented in [17], the model states are found weakly observable in a linear sense. An effective approach to enhance the observability is to incorporate algebraic constraints on the state variables into the estimator algorithm, so that the number of independent states can be reduced [29]. As discussed in [26], the PB-ECM-T preserves the feature of mass conservation of the P2D model. That is, the total number of lithium ions in the solid phase as well as in the electrolyte shall be constant when battery degradation is assumed ignorable during time period under investigation. However, as the ensemble is obtained using random generated perturbed states and measurement in in (12a) and (12b), the total amount n_{s} of lithium ions in the solid phase may differ from the initial value n_{s0}. Similarly, the total amount of the lithium ions n_{e} may differ from the initial value n_{e0}. To incorporate these physical constraints to the EnKF, $\forall p \in \{1, 2, \cdots, m\}$ and $\forall k > 0$, the solid phase and electrolyte concentrations are examined and updated following a scaling rule described below. For the sake of readability, the ensemble index p and the discrete time index k are dropped in the remaining part of this section.

First, for the solid phase concentrations, $\forall i \in \mathcal{S}^{\text{pos}} \cup \mathcal{S}^{\text{neg}}$, the scaling rule (14) is applied after each step of (12f):

1) Calculate the local average lithium ion concentration of the solid phase based on (10b),

$$\hat{c}_{s,\text{avg},i}^{+} = c_{s,\max,i}f_{\text{OCP},i}^{-1}(\hat{V}_{s,i}^{+}) \quad (14a)$$

where $\hat{V}_{s,i}^{+}$ is the ith member of $\hat{\mathbf{x}}_{k,p}^{+}$ for the positive electrode, and the $(N^{\text{pos}}+i)$th member of $\hat{\mathbf{x}}_{k,p}^{+}$ for the negative electrode.

2) Calculate the total amount of lithium ions n_{s} in the solid phase:

$$\hat{n}_{s}^{+} = \sum_{i \in \mathcal{S}^{\text{pos}}} \hat{c}_{s,\text{avg},i}^{+}\varepsilon_{s}^{\text{pos}}Al^{\text{pos}} + \sum_{i \in \mathcal{S}^{\text{neg}}} \hat{c}_{s,\text{avg},i}^{+}\varepsilon_{s}^{\text{neg}}Al^{\text{neg}} \quad (14b)$$

where ε_s is the volume fraction of the solid phase, and Al represents the volume of corresponding ES.

3) Update the local average concentration by scaling:

$$\hat{c}^+_{s,\text{avg},i,\text{update}} = \hat{c}^+_{s,\text{avg},i} \times \frac{n_{s0}}{\hat{n}^+_s}. \tag{14c}$$

4) Update the capacitor voltage

$$\hat{V}^+_{s,i,\text{update}} = f_{\text{OCP},i}\left(\hat{c}^+_{s,\text{avg},i,\text{update}}/c_{s,\text{max},i}\right) \tag{14d}$$

where $\hat{V}^+_{s,i,\text{update}}$ is the updated $\hat{V}^+_{s,i}$ considering the mass conservation. Similarly, the total amount of lithium ions n_e in the electrolyte is examined and updated via the scaling rule (15), i.e., $\forall i \in \mathcal{S}^{\text{pos}} \cup \mathcal{S}^{\text{sep}} \cup \mathcal{S}^{\text{neg}}$, based on (10c),

$$\hat{c}^+_{e,i} = c^0_e \exp\left(\frac{F}{2R_g t^0_a T}\hat{V}^+_{e,i}\right) \tag{15a}$$

where $\hat{V}^+_{e,i}$ is the $(N^{\text{pos}} + N^{\text{neg}} + i)$th member of $\hat{\mathbf{x}}^+_{k,p}$, and

$$\hat{n}^+_e = \sum_{i \in \mathcal{S}^{\text{pos}}} \hat{c}^+_{e,i}\varepsilon^{\text{pos}}_e Al^{\text{pos}} + \sum_{i \in \mathcal{S}^{\text{sep}}} \hat{c}^+_{e,i}\varepsilon^{\text{sep}}_e Al^{\text{sep}}$$
$$+ \sum_{i \in \mathcal{S}^{\text{neg}}} \hat{c}^+_{e,i}\varepsilon^{\text{neg}}_e Al^{\text{neg}} \tag{15b}$$

$$\hat{c}^+_{e,i,\text{update}} = \hat{c}^+_{e,i} \times \frac{n_{e0}}{\hat{n}^+_e} \tag{15c}$$

$$\hat{V}^+_{e,i,\text{update}} = \frac{2R_g t^0_a T}{F} \ln\left(\frac{\hat{c}^+_{e,i,\text{update}}}{c^0_e}\right) \tag{15d}$$

where ε_e is the porosity or the volume fraction of the electrolyte. The proposed EnKF (12) with the battery physical constraints (14) and (15) is hereafter denoted EnKF-c.

IV. RESULTS AND DISCUSSION

A. Model Validation

The model accuracy of the developed PB-ECM-T (11) in predicting battery behaviors shall first be examined. As the internal states and variables are difficult to be measured directly, the developed model was compared against the P2D-T model via simulation, as the rigorous P2D-based model has been widely accepted as a benchmark model for electrochemical Li-ion model validation. The detail of the P2D-T model is given in the supplementary material and the model parameters are from [26], [38]. The charge/discharge cycle is specified using an urban dynamometer driving schedule (UDDS) test relating to electric vehicle applications [39], with the original currents being scaled by a factor of about three. The resulted profile covers a large operating range for Li-ion batteries with a maximum current rate of 5.6 C. The model parameters are taken from [26], corresponding to a 1.8-Ah lithium-cobalt-oxide (LCO) battery cell. The rigorous P2D-T model was established in COMSOL Multiphysics 5.3a while the PB-ECM-T was implemented in MATLAB R2016a environment.

The simulation results from using these models are presented in Fig. 4 and Fig. 5. Padé approximation order is $M = 1$. The results using different number of ES, denoted $(N^{\text{pos}}, N^{\text{sep}}, N^{\text{neg}})$, are shown in Fig. 4. Clearly, the PB-ECM-T is able to match its high-order counterparts closely in
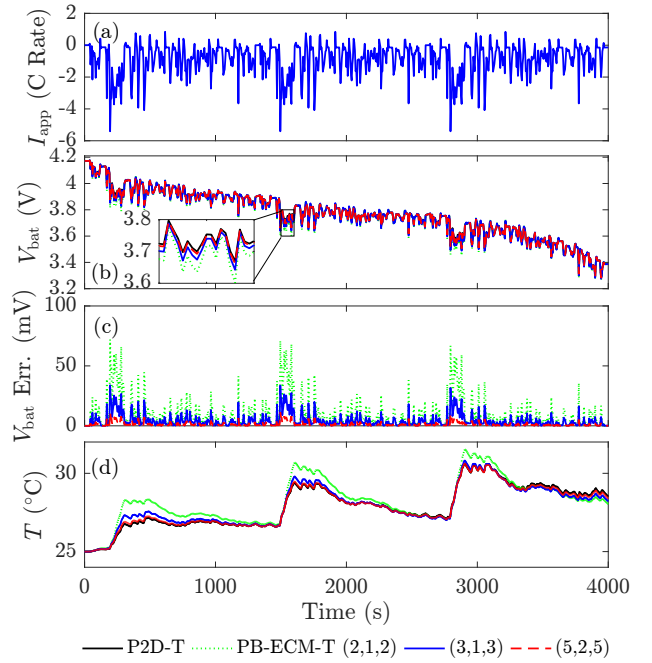

Fig. 4. Model comparison between the P2D-T model and the proposed PB-ECM-T $(N^{\text{pos}}, N^{\text{sep}}, N^{\text{neg}}) = (3, 1, 3)$: external behaviors of (a) applied current; (b) terminal voltage; (c) voltage error compared to the P2D-T model; (d) battery temperature.
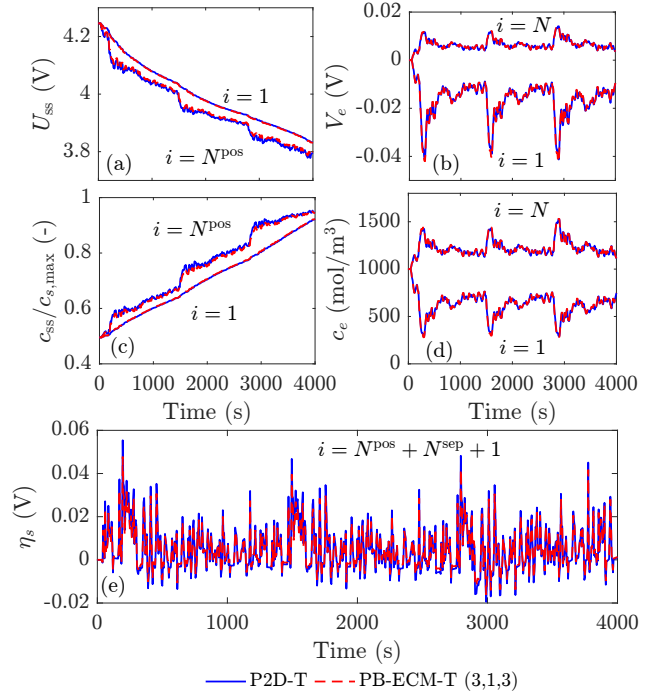

Fig. 5. Model comparison between the P2D-T model and the proposed PB-ECM-T $(N^{\text{pos}}, N^{\text{sep}}, N^{\text{neg}}) = (3, 1, 3)$: internal behaviors of (a) equilibrium potential of the electrode; (b) capacitor voltage V_e; (c) solid phase surface concentration; (d) electrolyte concentration; (e) activation overpotential.

terms of the terminal voltage and temperature across the entire operating process. Unsurprisingly, the accuracy of the model decreases when reducing $(N^{\text{pos}}, N^{\text{sep}}, N^{\text{neg}})$, i.e., the number of ES. However, even at $(N^{\text{pos}}, N^{\text{sep}}, N^{\text{neg}}) = (3, 1, 3)$, the

root-mean-square error (RMSE) of the terminal voltage is as low as 10.74 mV, and the maximum absolute error (MAE) is only about 37.9 mV. Interestingly, although not displayed in the figure, for the lowest ES number (1, 1, 1), the MAE of the battery voltage can reach high up to 0.15 V, which outperforms many of the empirical models in literature for such high-current rate profile. The error is due to the fact that the linear approximation of the derivative terms when implementing FVM becomes less valid when the number of control volumes reduces. The relationship between the number of ES and the simulated voltage errors are given in Table I. As mentioned earlier, to the structure of the PB-ECM-T, the number of states $n = (M + 1)(N^{pos} + N^{neg}) + N^{sep} + 1$. It can be seen that as the number of ES increases, voltage error can be reduced significantly, while the CPU time increases in a less radical manner. This shows the high computational efficiency of the PB-ECM even under large number of state variables thanks to the high sparsity of the state matrices of the circuit. Based on the results, we assume that $(N^{pos}, N^{sep}, N^{neg}) = (3, 1, 3)$ and $M = 1$ is the selection of the model complexity for the design of state estimator in the latter section.

Fig. 5 shows the results of the simulated internal variables which is related to internal limitation and degradation, where ES number is $(N^{pos}, N^{sep}, N^{neg}) = (3, 1, 3)$ and Padé order $M = 1$. The surface concentration in the negative electrode affect the rate of side reactions, while the overpotential has significant impact on the lithium plating during the period of overcharging. It is also observed that the most severe cases occur at the boundaries of each electrodes, and those variables shall be carefully considered in the design of optimal control of a battery system for real-time applications.

B. Performance of EnKF

In order to demonstrate the efficacy of the proposed distributed state estimator, the UDDS test with the current profile presented in Fig. 4(a) was used again. In the test, different ensemble sizes m are tested under both standard EnKF and EnKF-c estimators. The process noise covariance $\mathbf{Q}$ is assumed to be diagonal matrix and each of the element on the main diagonal equals 10^{-6}. The measurement noise covariance is assumed to be $\mathbf{R} = 1 \times 10^{-4}$, which corresponds to ± 10 mV voltage sensor error. To test the robustness and convergence speed of the employed estimation algorithm, the SOC are initialized with $SOC_0^{min} = 0.5$ and $SOC_0^{max} = 1$. In the simulations, the reference measurements are again generated by the PDAE-based battery model implemented in

TABLE I
MODEL ACCURACY AND SPEED OF THE PB-ECM WITH DIFFERENT NUMBERS OF ES

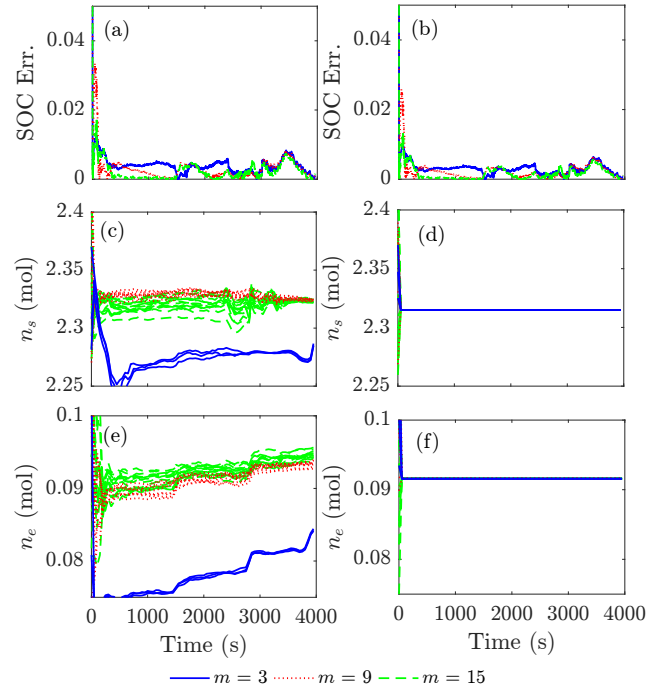| Number of ES $(N^{pos}, N^{sep}, N^{neg})$	Number of States n	RMSE (mV)	MAE (mV)	CPU Time (s)
(2, 1, 2)	10	10.74	76.7	1.4
(3, 1, 3)	14	4.86	37.9	1.6
(5, 2, 5)	23	1.73	14.6	1.9
(7, 3, 7)	32	0.83	7.3	2.1
(10, 5, 10)	46	0.35	3.1	2.9
(20, 10, 20)	91	0.09	0.93	5.1

Fig. 6. Effect of ensemble size and constraint on mass conservation: (a) SOC estimation error based on EnKF; (b) SOC estimation error based on EnKF-c; (c) total amount of lithium ions in the solid phase based on EnKF; (d) total amount of lithium ions in the solid phase based on EnKF-c; (c) total amount of lithium ions in the electrolyte based on EnKF; (d) total amount of lithium ions in the electrolyte based on EnKF-c.

COMSOL Multiphysics. The sampling time for EnKF design is chosen to be $\Delta t = 1$ s. The performances of the EnKF estimators with different m are shown in Table II. It can be seen that there is an approximately linear relationship between the ensemble size and the execution time for both EnKF and EnKF-c. For EnKF-c, the 9.5 s execution time for this 4000 s UDDS profile (i.e., 2.4 ms per time-step) is affordable for online operation.

TABLE II
COMPARISON ENKFS WITH DIFFERENT ENSEMBLE SIZES

Ensemble Size m	RMSE of SOC (%)		Execution Time (s)	
	EnKF	EnKF-c	EnKF	EnKF-c
3	0.77	0.33	8.3	9.5
9	0.61	0.31	11.7	13.3
15	0.38	0.31	16.6	18.1
21	0.33	0.30	19.5	21.2
27	0.29	0.29	23.1	25.3

Fig. 6 shows the effects of varying the ensemble size and the mass conservation constraint on the EnKF performance. First, as the ensemble size increases, both the accuracy of SOC prediction and the speed of convergence increase. However, when the ensemble size is large (e.g. $m = 15$), the effect of introducing this constraint is not tangible. Hence, for small-size ensemble (e.g. $m = 3$) improved numerical efficiency, it is advantageous to introduce the constraint on mass conservation.

The performance of the EnKF to predict the health-related internal variables with $m = 3$ is shown in Fig. 7. It can be seen that although a large initial deviation has been introduced,
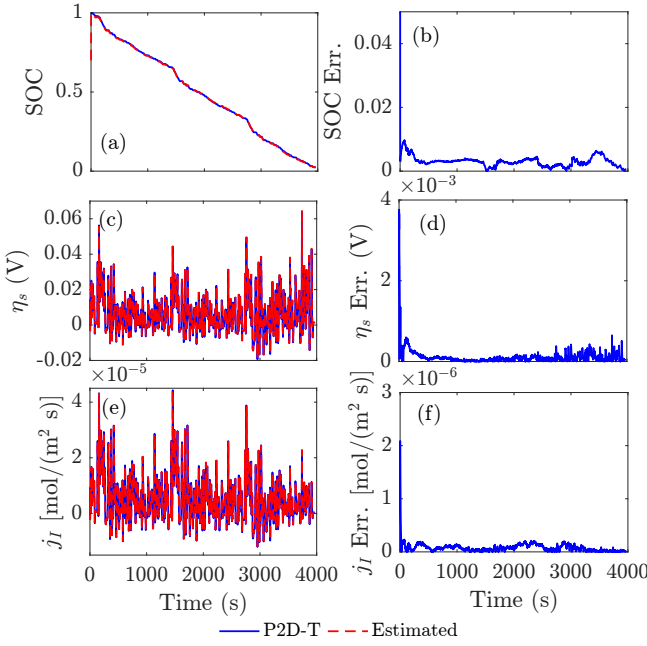
Fig. 7. Performance of PB-ECM-T-based EnKF-c for internal state estimation (ensemble size $m = 3$). (a) SOC; (b) estimation error of SOC; (c) activation overpotential at ES index $i = N^{\text{pos}} + N^{\text{sep}} + 1$; (d) estimation error of the overpotential; (e) intercalation molar flux at ES index $i = N^{\text{pos}} + N^{\text{sep}} + 1$; (f) estimation error of the molar flux.
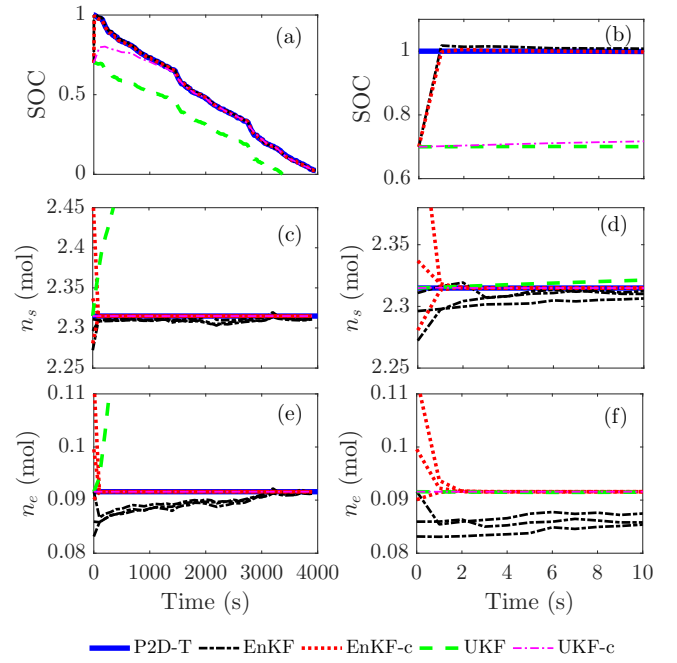

Fig. 8. Comparison of performance of different nonlinear state estimators: (a)(b) SOC; (c)(d) total amount of lithium ions in the solid phase; (e)(f) total amount of lithium ions in the electrolyte.

the solution of the EnKF-c is able to rapidly converge to its true value. From Fig. 7(b), it can be seen that the MAE for SOC after 100 s is 0.95%, and the RMSE is 0.33%, which indicates the superior performance on SOC estimation. In the meanwhile, the estimation errors on health-related variables are also very small, which can be observed from Figs. 7(c)–(f).

C. Comparative Studies with Other Nonlinear Estimators

Based on sequential linearization, EKF adopts the first-order approximation of the nominal model (11) for gain calculation and covariance propagation. By contrast, UKF executes the second-order approximation of the nominal model via an unscented transform. Thus, it is easy to understand that UKF generally has higher accuracy than EKF if (11) well predicts the battery system. As explained earlier, based upon (11), EKF can be inferior in computational efficiency due to the need to calculate a set of Jacobian matrices online. With this in mind, a standard UKF estimator without any physical constraints and a UKF estimator considering the mass conservation (UKF-c) are designed based on PB-ECM-T to benchmark the proposed estimator, whereas the numerical comparison with EKF will not be considered.

TABLE III
COMPARISON OF ENKF- AND UKF-BASED STATE ESTIMATORS

	EnKF	EnKF-c	UKF	UKF-c
Ensemble Size or No. of Sigma Points	3	3	29	29
RMSE of SOC (%)	0.77	0.33	28.5	3.1
Convergence Time (s)*	4	3	1135	-
Execution Time (s)	8.3	9.5	29.2	37.6

*Defined as the time when SOC estimation error reaches 1%.

For the UKF-c, the constraint of mass conservation is also taken into consideration during the generation of the sigma points of the standard UKF algorithm following the steps similar to (14) and (15). The ensemble sizes for the EnKF and the EnKF-c are both $m = 3$. The simulation results under UDDS test are shown in Fig. 8, where the left column compares the performance over the 4000 s simulation time and the right column shows the initialization processes. It can be seen from Fig. 8(a) that there are large persistent estimation errors for the standard UKF estimator, and the UKF-c estimator requires a long period of time ($>$1000 s) to converge to the true SOC value. In contrast, for the EnKF and EnKF-c, the convergence time is very short, thanks to the proposed ensemble initialization method (13). Furthermore, as can be observed in Fig. 8(d) and Fig. 8(f), the application of the physical constraints guarantees the mass conservation for both EnKF-c and UKF-c. However, while UKF-c algorithm requires $2n + 1 = 29$ sigma points, the EnKF-c estimator requires an ensemble with only three samples. The execution time given in Table III shows that the execution time 37.6 s of the UKF-c is about four times longer than that of the EnKF-c estimator. Moreover, EnKF-c can provide much faster convergence and higher estimation accuracy than its counterpart. Hence, it can be concluded that the proposed EnKF-c is effective and efficient in the presence of a range of common uncertainties from modeling, initialization, and persistent noise.

V. CONCLUSIONS

This work proposes a novel distributed electrochemical state estimation method for lithium-ion (Li-ion) batteries using a sophisticated physics-based equivalent circuit model derived from an electrochemical-thermal coupled pseudo-two-

dimensional model. A nonlinear state-space representation of the battery model is obtained by reformulating the system into a circuit network with simplified thermal behavior for the ease of control system implementation. The developed model is capable of accurately reflecting the internal behaviors and operating limitations of the Li-ion battery with low computational cost. A constrained ensemble Kalman filter (EnKF) is designed to monitoring the internal distributed states with low computational burden for online operation. A simple ensemble initialization method and physical constraints on mass conservation are incorporated into the EnKF algorithm to address the problem of slow convergence due to the weak observability of the battery model. The performance of the proposed distributed state estimator is validated and compared with unscented Kalman filter based approaches. Simulation results show that the proposed EnKF-based estimator provides much superior performance, while model's capability to accurately monitor the internal variables can be utilized for the design of optimal control schemes in the future development of health-aware battery management systems. Further improvement of the proposed method can be achieved by incorporating the degradation dynamics and estimating the unknown error covariance adaptively in the future works.

REFERENCES

[1] M. T. Lawder *et al.*, "Battery energy storage system (BESS) and battery management system (BMS) for grid-scale applications," *Proc. IEEE*, vol. 102, no. 6, pp. 1014–1030, Jun. 2014.

[2] Y. Li, M. Vilathgamuwa, S. S. Choi, T. W. Farrell, N. T. Tran, and J. Teague, "Development of a degradation-conscious physics-based lithium-ion battery model for use in power system planning studies," *Appl. Energy*, vol. 248, pp. 512–525, Aug. 2019.

[3] N. A. Chaturvedi, R. Klein, J. Christensen, J. Ahmed, and A. Kojic, "Algorithms for advanced battery-management systems," *IEEE Control Syst. Mag.*, vol. 30, no. 3, pp. 49–68, Jun. 2010.

[4] S. Nejad, D. T. Gladwin, and D. A. Stone, "A systematic review of lumped-parameter equivalent circuit models for real-time estimation of lithium-ion battery states," *J. Power Sources*, vol. 316, pp. 183–196, Jun. 2016.

[5] G. Dong, F. Yang, Z. Wei, J. Wei, and K. Tsui, "Data-driven battery health prognosis using adaptive Brownian motion model," *IEEE Trans. Ind. Informat.*, to be published.

[6] R. R. Richardson, C. R. Birkl, M. A. Osborne, and D. A. Howey, "Gaussian process regression for in situ capacity estimation of lithium-ion batteries," *IEEE Trans. Ind. Informat.*, vol. 15, no. 1, pp. 127–138, Jan. 2019.

[7] C. Zou, C. Manzie, and D. Nešić, "Model predictive control for lithium-ion battery optimal charging," *IEEE/ASME Trans. Mechatron.*, vol. 23, no. 2, pp. 947–957, Apr. 2018.

[8] Y. Gao *et al.*, "Health-aware multi-objective optimal charging strategy with coupled electrochemical-thermal-aging model for lithium-ion battery," *IEEE Trans. Ind. Informat.*, vol. 16, no. 5, pp. 3417–3429, May 2020.

[9] M. Doyle and J. Newman, "Modeling the performance of rechargeable lithium-based cells: Design correlations for limiting cases," *J. Power Sources*, vol. 54, no. 1, pp. 46–51, Mar. 1995.

[10] S. Santhanagopalan, Q. Guo, P. Ramadass, and R. E. White, "Review of models for predicting the cycling performance of lithium ion batteries," *J. Power Sources*, vol. 156, no. 2, pp. 620–628, Jun. 2006.

[11] S. Santhanagopalan and R. E. White, "Online estimation of the state of charge of a lithium ion cell," *J. Power Sources*, vol. 161, no. 2, pp. 1346–1355, Oct. 2006.

[12] D. Di Domenico, A. Stefanopoulou, and G. Fiengo, "Lithium-ion battery state of charge and critical surface charge estimation using an electrochemical model-based extended Kalman filter," *J. Dyn. Syst. Meas. Control*, vol. 132, no. 6, pp. 061 302–1–061 302–11, Nov. 2010.

[13] S. Dey and B. Ayalew, "Nonlinear observer designs for state-of-charge estimation of lithium-ion batteries," in *Amer. Control Conf.*, Portland, OR, USA, Jun. 4-6, 2014, pp. 248–253.

[14] Y. Wang, H. Fang, Z. Sahinoglu, T. Wada, and S. Hara, "Adaptive estimation of the state of charge for lithium-ion batteries: Nonlinear geometric observer approach," *IEEE Trans. Control Syst. Technol.*, vol. 23, no. 3, pp. 948–962, May 2015.

[15] S. Santhanagopalan and R. E. White, "State of charge estimation using an unscented filter for high power lithium ion cells," *Int. J. Energy Res.*, vol. 34, no. 2, pp. 152–163, Feb. 2010.

[16] S. J. Moura, F. B. Argomedo, R. Klein, A. Mirtabatabaei, and M. Krstic, "Battery state estimation for a single particle model with electrolyte dynamics," *IEEE Trans. Control Syst. Technol.*, vol. 25, no. 2, pp. 453–468, Mar. 2017.

[17] C. Zou, X. Hu, Z. Wei, T. Wik, and B. Egardt, "Electrochemical estimation and control for lithium-ion battery health-aware fast charging," *IEEE Trans. Ind. Electron.*, vol. 65, no. 8, pp. 6635–6645, Aug. 2018.

[18] R. Klein, N. A. Chaturvedi, J. Christensen, J. Ahmed, R. Findeisen, and A. Kojic, "Electrochemical model based observer design for a lithium-ion battery," *IEEE Trans. Control Syst. Technol.*, vol. 21, no. 2, pp. 289–301, Jan. 2011.

[19] A. M. Bizeray, S. Zhao, S. R. Duncan, and D. A. Howey, "Lithium-ion battery thermal-electrochemical model-based state estimation using orthogonal collocation and a modified extended Kalman filter," *J. Power Sources*, vol. 296, pp. 400–412, Nov. 2015.

[20] M. Corno, N. Bhatt, S. M. Savaresi, and M. Verhaegen, "Electrochemical model-based state of charge estimation for Li-ion cells," *IEEE Trans. Control Syst. Technol.*, vol. 23, no. 1, pp. 117–127, Jan. 2015.

[21] J. Sturm, H. Ennifar, S. V. Erhard, A. Rheinfeld, S. Kosch, and A. Jossen, "State estimation of lithium-ion cells using a physicochemical model based extended Kalman filter," *Appl. Energy*, vol. 223, pp. 103–123, Aug. 2018.

[22] K. A. Smith, C. D. Rahn, and C.-Y. Wang, "Model-based electrochemical estimation and constraint management for pulse operation of lithium ion batteries," *IEEE Trans. Control Syst. Technol.*, vol. 18, no. 3, pp. 654–663, May 2010.

[23] K. D. Stetzel, L. L. Aldrich, M. S. Trimboli, and G. L. Plett, "Electrochemical state and internal variables estimation using a reduced-order physics-based model of a lithium-ion cell and an extended Kalman filter," *J. Power Sources*, vol. 278, pp. 490–505, Mar. 2015.

[24] M.-T. von Srbik, M. Marinescu, R. F. Martinez-Botas, and G. J. Offer, "A physically meaningful equivalent circuit network model of a lithium-ion battery accounting for local electrochemical and thermal behaviour, variable double layer capacitance and degradation," *J. Power Sources*, vol. 325, pp. 171–184, Sep. 2016.

[25] Y. Merla, B. Wu, V. Yufit, R. F. Martinez-Botas, and G. J. Offer, "An easy-to-parameterise physics-informed battery model and its application towards lithium-ion battery cell design, diagnosis, and degradation," *J. Power Sources*, vol. 384, pp. 66–79, Apr. 2018.

[26] Y. Li, M. Vilathgamuwa, T. Farrell, S. S. Choi, N. T. Tran, and J. Teague, "A physics-based distributed-parameter equivalent circuit model for lithium-ion batteries," *Electrochimica Acta*, vol. 299, pp. 451–469, Mar. 2019.

[27] N. T. Tran, M. Vilathgamuwa, Y. Li, T. Farrell, S. S. Choi, and J. Teague, "A computationally-efficient electrochemical-thermal model for small-format cylindrical lithium ion batteries," in *Proc. 4th IEEE Southern Power Electron. Conf.*, Singapore, Dec. 10-13, 2018, pp. 1–7.

[28] A. Tulsyan, Y. Tsai, R. B. Gopaluni, and R. D. Braatz, "State-of-charge estimation in lithium-ion batteries: A particle filter approach," *J. Power Sources*, vol. 331, pp. 208–223, Nov. 2016.

[29] S. Marelli and M. Corno, "A soft-constrained unscented Kalman filter estimator for Li-ion cells electrochemical model," in *Proc. 56th IEEE Conf. Decis. Control*, Melbourne, VIC, Australia, Dec. 12-15, 2017, pp. 1535–1540.

[30] G. Evensen, "Sequential data assimilation with a nonlinear quasi-geostrophic model using Monte Carlo methods to forecast error statistics," *J. Geophys. Res. Oceans*, vol. 99, no. C5, pp. 10 143–10 162, May 1994.

[31] G. Evensen, "The ensemble Kalman filter for combined state and parameter estimation," *IEEE Control Syst. Mag.*, vol. 29, no. 3, pp. 83–104, Jun. 2009.

[32] Y. M. Ruckstuhl and T. Janjić, "Parameter and state estimation with ensemble Kalman filter based algorithms for convective-scale applications," *Quart. J. Roy. Meteorol. Soc.*, vol. 144, no. 712, pp. 826–841, Feb. 2018.

[33] D. Simon, "Kalman filtering with state constraints: a survey of linear and nonlinear algorithms," *IET Control Theory Appl.*, vol. 4, no. 8, pp. 1303–1318, Aug. 2010.

[34] J. C. Forman, S. Bashash, J. L. Stein, and H. K. Fathy, "Reduction of an electrochemistry-based Li-ion battery model via quasi-linearization and

Padé approximation," *J. Electrochem. Soc.*, vol. 158, no. 2, pp. A93–A101, Feb. 2011.

[35] N. T. Tran, M. Vilathgamuwa, T. Farrell, S. S. Choi, Y. Li, and J. Teague, "A Padé approximate model of lithium ion batteries," *J. Electrochem. Soc.*, vol. 165, no. 7, pp. A1409–A1421, May 2018.

[36] H. Fang, N. Tian, Y. Wang, M. Zhou, and M. A. Haile, "Nonlinear Bayesian estimation: from Kalman filtering to a broader horizon," *IEEE/CAA J. Autom. Sinica*, vol. 5, no. 2, pp. 401–417, Mar. 2018.

[37] F. Zhang, C. Snyder, and J. Sun, "Impacts of initial estimate and observation availability on convective-scale data assimilation with an ensemble Kalman filter," *Monthly Weather Rev.*, vol. 132, no. 5, pp. 1238–1253, May 2004.

[38] M. Torchio, L. Magni, R. B. Gopaluni, R. D. Braatz, and D. M. Raimondo, "LIONSIMBA: A Matlab framework based on a finite volume model suitable for Li-ion battery design, smulation, and control," *J. Electrochem. Soc.*, vol. 163, no. 7, pp. A1192–A1205, Jan. 2016.

[39] The EPA urban dynamometer driving schedule (UDDS). [Online]. Available: https://www.epa.gov/vehicle-and-fuel-emissions-testing/dynamometer-drive-schedules

Yang Li (Member, IEEE) received the B.E. degree in electrical engineering from Wuhan University, Wuhan, China, in 2007, and the M.Sc. and Ph.D. degrees in power engineering from Nanyang Technological University (NTU), Singapore, in 2008 and 2015, respectively.

From 2015 to 2016, he was a Research Fellow with the Energy Research Institute, NTU. From 2016 to 2018, he was a Research Fellow with the School of Electrical Engineering and Computer Science, Queensland University of Technology, Brisbane, QLD, Australia. Since 2019, he has been with the School of Automation, Wuhan University of Technology, Wuhan. He is currently a Visiting Professor with the Department of Electrical Engineering, Chalmers University of Technology, Gothenburg, Sweden. His research interests include modeling and control of energy storage systems in power grid and transport sectors.

Dr. Li is a recipient of the EU Marie Skłodowska-Curie Action Individual Fellowships in 2020.

Binyu Xiong (Member, IEEE) received the B.E. degree in electrical engineering from Wuhan University, Wuhan, China, in 2010, and the M.Sc. and Ph.D. degrees in power engineering from Nanyang Technological University, Singapore, in 2011 and 2016, respectively. He is currently an Associate Professor with the School of Automation, Wuhan University of Technology, Wuhan.

His research interests include electrical and thermal modeling of batteries, battery state of charge estimation, large-scale energy storage systems, and renewable energy generations.

Don Mahinda Vilathgamuwa (Fellow, IEEE) received the B.Sc. degree from the University of Moratuwa, Sri Lanka, in 1985, and the Ph.D. degree from Cambridge University, Cambridge, U.K., in 1993, both in electrical engineering.

In 1993, he joined the School of Electrical and Electronic Engineering, Nanyang Technological University, Singapore, where he had been a Faculty Member until 2013. He is currently a Professor of power engineering with Queensland University of Technology, Brisbane, Australia. His research interests include wireless power, battery storage, power electronic converters, electrical drives, and electromobility.

Dr. Vilathgamuwa was an Associate Editor for the IEEE TRANSACTIONS ON INDUSTRY APPLICATIONS from 2014 to 2017. He is an Associate Editor for the IEEE TRANSACTIONS ON INDUSTRIAL ELECTRONICS. He is currently the Chairman of IEEE Industry Applications/Power Electronics/Industrial Electronics Society Joint Chapter in Queensland, Australia.

Zhongbao Wei (Member, IEEE) received the B.Eng. and M.Sc. degrees in instrumental science and technology from Beihang University. Beijing, China, in 2010 and 2013, respectively, and the Ph.D. degree in power engineering from Nanyang Technological University, Singapore, in 2017.

He was a Research Fellow with the Energy Research Institute, Nanyang Technological University, from 2016 to 2018. He is currently a Professor of vehicle engineering with National Engineering Laboratory for Electric Vehicles, School of Mechanical Engineering, Beijing Institute of Technology, Beijing. He has authored more than 40 peer-reviewed articles. His research interests include battery modeling, identification, state estimation, diagnostic, and thermal management, with applications to renewable energy systems such as lithium-ion battery and vanadium redox flow battery.

Changjun Xie (Member, IEEE) received the Ph.D. degree in vehicle engineering from Wuhan University of Technology (WUT), Wuhan, China in 2009.

From 2012 to 2013, he was a Visiting Scholar with the University of California, Davis, CA, USA. He is currently a Professor of electrical engineering with the School of Automation, WUT, where he is also the Vice Dean of the School of Automation and the Director of the Institute of New Energy Detection and Control Technology. He has authored more than 50 peer-reviewed articles. His research interests include battery management, control, and optimization of new energy vehicles.
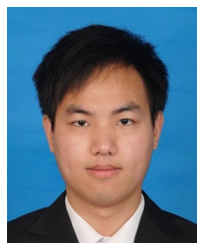
Changfu Zou (Member, IEEE) received the B.E. degree in automotive engineering from the Beijing Institute of Technology, Beijing, China, in 2011, and the Ph.D. degree in automation and control engineering from the Department of Mechanical Engineering, University of Melbourne, VIC, Australia, in 2017. He was a Postdoctoral Researcher with the Chalmers University of Technology, Gothenburg, Sweden, where he is currently an Assistant Professor with the Automatic Control Group, Department of Electrical Engineering. He was a Visiting Student Researcher with the Energy, Controls and Applications Laboratory, University of California, Berkeley, CA, USA, from 2015 to 2016. His research interests include modeling and control of energy storage systems, electrified vehicles, and transport systems.

Dr. Zou was a recipient of the Swedish Research Council Starting Grant, the Melbourne Research Scholarship, the Scholarship of National ICT Australia, and Excellent Graduate Award of Beijing.